RSC Advances

PAPER

View Article Online
View Journal | View Issue

Cite this: *RSC Adv.*, 2023, **13**, 13575

Microstructure-driven electrical conductivity optimization in additively manufactured microscale copper interconnects†

Maxence Menétrey, ‡[a] Cathelijn van Nisselroy,‡[b] Mengjia Xu,[b] Julian Hengsteler,[b] Ralph Spolenak*[a] and Tomaso Zambelli *[b]

Received 29th January 2023
Accepted 4th April 2023

DOI: 10.1039/d3ra00611e

rsc.li/rsc-advances

As the microelectronics field pushes to increase device density through downscaling component dimensions, various novel micro- and nano-scale additive manufacturing technologies have emerged to expand the small scale design space. These techniques offer unprecedented freedom in designing 3D circuitry but have not yet delivered device-grade materials. To highlight the complex role of processing on the quality and microstructure of AM metals, we report the electrical properties of micrometer-scale copper interconnects fabricated by Fluid Force Microscopy (FluidFM) and Electrohydrodynamic-Redox Printing (EHD-RP). Using a thin film-based 4-terminal testing chip developed for the scope of this study, the electrical resistance of as-printed metals is directly related to print strategies and the specific morphological and microstructural features. Notably, the chip requires direct synthesis of conductive structures on an insulating substrate, which is shown for the first time in the case of FluidFM. Finally, we demonstrate the unique ability of EHD-RP to tune the materials resistivity by one order of magnitude solely through printing voltage. Through its novel electrical characterization approach, this study offers unique insight into the electrical properties of micro- and submicrometer-sized copper interconnects and steps towards a deeper understanding of micro AM metal properties for advanced electronics applications.

1 Introduction

Additive manufacturing (AM) has become a widespread manufacturing strategy by offering unique opportunities in the way materials are designed and manufactured. While AM of macroscopic parts readily entered the stage of industrial fabrication, the path towards AM of micro- and nanoscale objects currently is a flourishing field of research,[1,2] opening the door to breakthrough innovations in the design of microelectronics, such as complex conductive circuits,[3,4] or 3D micro-sensors.[5,6] Nonetheless, for AM to make a significant impact in the fabrication of such components, it has to deliver conductive elements with well-controlled resistivity. In metals, this property is dictated by electron scattering and can be empirically approximated as the sum of the contributions of individual scattering mechanisms. In bulk materials, scattering events occur primarily due to impurities, thermal vibrations, and lattice defects (grain boundaries, dislocations, point defects). In small objects, however, scattering at interfaces (*i.e.* surfaces) further impacts the electrical performance as soon as one dimension is on the order of the electron mean free path.[7] This phenomenon, known as the classical size effect, leads to inferior electrical performance in downsized electronics and microscale devices of particular interest in the semiconductor industry.[8] For nanometer-sized conductors, the electron scattering is dominated by interfacial scattering which is generally described by the Fuchs and Sondheimer (FS) model, and grain boundary scattering where Mayadas and Shatzkes (MS) model[9] is widely applied to explain resistivity.[10]

To date, microscale AM methods are not ready to deliver materials competing at the same time with the resolution of lithography processes and the purity of thin film deposition technologies. Nonetheless, particle-based transfer techniques generally achieve crystalline microstructure (despite the presence of pores) after annealing, and electrochemistry-based techniques display as-deposited dense and crystalline metal microstructures with mechanical properties reaching that of thin film technologies.[11] Moreover, the extensive microstructure tuning reported by micro AM techniques appears to be a unique asset, first by offering potential in terms of materials optimization, and second by allowing spatial modulations in

[a]*Laboratory for Nanometallurgy, Department of Materials, ETH Zürich, Vladimir-Prelog-Weg 1-5/10, 8093 Zürich, Switzerland. E-mail: ralph.spolenak@mat.ethz.ch*

[b]*Laboratory of Biosensors and Bioelectronics, Department of Information Technology and Electrical Engineering, ETH Zürich, Gloriastrasse 35, 8092 Zürich, Switzerland. E-mail: ztomaso@ethz.ch*

† Electronic supplementary information (ESI) available. See DOI: https://doi.org/10.1039/d3ra00611e

‡ These authors contributed equally to this work.

Table 1 Overview of reported resistivity values by state-of-the-art micro AM approaches for different metals. Larger than bulk is the ratio between the measured resistivity and that of the bulk, while smallest dim. is the shortest dimension in the cross-sectional area of the measured structure

Method	Metal	Resistivity μΩ cm	Larger than bulk (*ca.*)	Measurement configuration	Smallest dim. (*ca.*) μm	Ref.
EHD	Au	5–20	2.5–10	4-Terminal	0.2	18
	Au	88	36	2-Terminal	0.5	17
	Ag	30	20	2-Terminal	1.7	16
	Cu	5.98–24.2	3–15	2-Terminal	0.1	15
LIFT	Cu	18.7–35.3	11–22	2-Terminal	2.2	24
	Ag	1.9	1.2	4-Terminal	5.0	23
DIW	Ag	5.4	3.5[a]	4-Terminal	15	13
	Ag	5	3	[b]	25	20
	Ag	5–9.5	3–6	2-Terminal	4	21
	Cu	3.2	2	2-Terminal	[b]	22
MCED	Cu	1150	680	4-Terminal	0.5	25
	Cu	649	389	2-Terminal	11	26
	Cu	31.5	19	4-Terminal	0.5	27
	Cu	39	23	2-Terminal	1	30
	Cu	3.1	1.9	2-Terminal	0.74	29
	Cu	63.6	38	2-Terminal	0.76	28
EHD-RP	Cu	14.4	8.6	2-Terminal	0.15	32
	Cu	70–555	41–330	4-Terminal	0.14	This study
FluidFM	Cu	30–662	18–394	4-Terminal	0.9	This study

[a] The resistivity can be tuned up to three orders of magnitude (with respect to bulk silver) by changing the laser intensity. [b] The value or information is not reported.

properties though on-the-fly adjustments in processing parameters.[12,13] Thus, to take advantage of this opportunity and make the step towards microelectronics application, an advanced understanding of the causal relationship that link printing strategy, processing parameters to the resulting electrical performance is required. Despite this critical need, no study has undertaken such comprehensive approach. Instead, the majority of scientific work touching upon electrical properties of micro AM objects report on a limited amount of data; often only a single line or pillar is characterized (Table 1). What is further missing for such a study is a standardized measurement template allowing fair comparison between printed microscale conductors.

We here report on the electrical characterization of copper micro- and submicrometer-sized interconnects printed by two different microscale AM techniques—namely FluidFM and EHD-RP. The introduction of a standardized thin film-based electrode testing chip allows reliable comparison of electrical properties, attributed to different printing strategies, and deposited metal microstructures. Notably both techniques, despite relying on an electrochemical reduction and therefore an electrical current, achieve the deposition of conductive structures on and across an insulating substrate. Finally, following the recent report on precise grain-size control by EHD-RP and its influence on mechanical properties,[12] we demonstrate, how similar strategies can be employed to extensively tune the as-deposited copper resistivity. In order to introduce the background of the study, we first provide a short review of the electrical properties of metal micro-objects fabricated by various state-of-the-art micro AM techniques.

1.1 Review on electrical conductivity of microscale metal AM

In the scope of comparing electrical performance, microscale metal AM methods can be advantageously categorized into transfer techniques (relying on the local deposition of pre-synthesized materials) and synthesis techniques (where materials are synthesized *in situ* from metal ions or other precursors) because the microstructure of the deposit strongly depends on the fabrication type.[1] The resistivity values reported in the literature for metal synthesized by micro AM techniques are summarized in Table 1.

Transfer techniques mostly lead to the deposition of particles aggregates and thus require an annealing step in order to approach bulk properties.[11] Electrohydrodynamic (EHD) printing of inks is based on the rapid ejection of nanodroplets containing metal nanoparticles from a pipette nozzle.[14] Upon impact on the substrate, the volatile components of the ink evaporate, leaving as-deposited nanoparticles behind. In this manner, copper tracks, silver bridges and gold wires were 3D printed with resistivity values about one order of magnitude higher than bulk.[15–17] Recently, fabrication and electrical characterization of high-aspect-ratio gold nanowalls under atmospheric conditions were reported.[18] After sintering, the nanowalls exhibited a resistivity approaching bulk gold. Ejection of silver nanoparticles-loaded inks by direct ink writing (DIW) resulted in the 3D printing of various geometries with applications in radio-frequency (RF)- and microelectronics, with resistivity values of 3× to 15× bulk silver.[19–21] As a mean to extend materials properties tunability, laser-assisted DIW—combining DIW with local on-the-fly laser sintering—allowed for the fabrication of segmented silver wires with tailored

electrical resistivity ranging from three up to three orders of magnitude larger than bulk.[13] Additionally, electroless deposition (ELD) assisted DIW of copper 3D micro-circuitries reported a resistivity reaching as low as 2× of bulk value.[22] Laser-induced forward transfer (LIFT) of nanopastes could produce dense silver voxels of varying dimensions that were stacked to create wirebonds connecting a LED circuit on a polyimide substrate.[23] Curing the as-deposited paste at 250 °C for one hour decreased the resistivity by three orders or magnitude, thereby approaching the bulk value (1.2× higher). Microstructural analysis revealed an increase in average grain size with annealing temperature from 70 nm (150 °C) to 200 nm (250 °C) which, together with the removal of organic components detected by thermogravimetric analysis, explained the decrease in resistivity from 6.7 μΩ cm down to 1.9 μΩ cm. In a similar work on LIFT, stacking of solidified copper droplets enabled the fabrication of high aspect-ratio pillars with resistivity values reaching 10× and 30× bulk copper, for deposition in argon atmosphere and air respectively.[24]

Synthesis techniques, and in particular localized electrodeposition, have the ability to synthesize dense and crystalline metals and do not necessarily require a post-printing annealing step.[11] Yet, electrical performance varies considerably among the different works. Copper micro-objects manufactured by meniscus confined electrodeposition (MCED) reported resistivity values ranging from 2 to 3 orders of magnitude larger[25,26] down to ≈20× larger[27,28] than bulk copper, to as low as just twice bulk resistivity.[29] In the latter study, in addition to copper, platinum wirebonds were printed which revealed a linear ohmic behavior at low currents, transitioning to a non-ohmic regime for higher currents due to Joule heating. Recently, 3D printed nanotwinned copper engineered by localized pulsed electrodeposition (LPED) exhibited a remarkable trade-off in mechanical and electrical properties, reaching only ≈20× bulk resistivity.[30] Interestingly, the resistivity was nearly half of its direct current (DC) counterpart, which is a pattern also reported for the PED of 2D copper foils.[31] Besides the various types of MCED mentioned above, Electrohydrodynamic-Redox 3D Printing (EHD-RP) produced dense and polycrystalline copper lines with the lowest resistivity values of 14.4 μΩ cm, corresponding to 8.6× bulk copper.[32]

2 Results & discussion

2.1 Working principles

2.1.1 FluidFM. FluidFM is a 3D printing technology related to scanning probe lithography[33] combining microfluidics with atomic force microscopy (AFM).[34] Instead of employing standard AFM cantilevers, the FluidFM uses a specific probe that has a hollow microfluidic channel running all the way from the tip apex to the probe's reservoir, which is in turn connected to an external pressure controller. The hollow probe is mounted onto a standard AFM and therefore benefits not only from the scanning probe capabilities but also from the system's integrated force feedback. The probe is filled with a metal salt solution (the printing "ink") and placed inside a droplet cell, a three-electrode electrochemical cell immersed in liquid. Since the cell's working electrode is a negatively biased gold-coated substrate, electrochemical reduction of the locally dispensed ions is enabled, leading to the deposition of confined metal voxels (see Fig. 2(a)). The height of each metal voxel is controlled using the built-in force feedback mechanism of the AFM: upon growing, the metal deposit reaches the tip apex and the resulting deflection of the cantilever (and thus the laser beam) induces a voltage shift in the system's photo-diode. The in-house developed software interprets this event as the completion of the requested voxel and steers the probe to the next printing location. This approach allows for true layer-by-layer or voxel-by-voxel printing of metal designs as depicted in Fig. 2(a).[35,36]

2.1.2 EHD-RP. EHD-RP technique—schematized in Fig. 2(c)—was first introduced by Reiser *et al.*[32] and combines forced mass transfer (EHD ejection from a quartz capillary nozzle) with *in situ* materials synthesis (confined electrodeposition). A voltage of ≈100 V applied between an immersed sacrificial anode and the grounded substrate (typical distance: ≈10 μm) triggers two processes happening in parallel: first, the metal anode oxidation, leading to the release of solvated metal ions; second, the EHD ejection of ion-loaded solvent droplets from a sub-micrometer-sized capillary nozzle towards the substrate. Upon landing, the ions are reduced while the organic solvent quickly evaporates, giving rise to sub-micrometric metal voxels.

2.2 Substrate with built-in electrodes

To enable facile and standardized comparison of electrical characterization of conductive AM structures, this study designed an electrode chip with 8 sample testing areas (*i.e.* subchips), each of which comprising 9 sets of 4 elongated thin-film electrodes (Fig. 1(a)). A conductive structure is printed across each set of electrodes, Fig. 1(c), allowing 4-terminal electrical characterization, which obviates any contribution of the contact resistance to the measurement. The electrodes gradually diverge towards larger pads which are easily contacted by microprobes, thereby facilitating parametric studies (72 measurements per chip). These chips are produced *via* lithography-patterning (Fig. 1(b)) for superior consistency in probe contact as compared to contact electrodes added post-printing by focus ion beam-induced deposition. The design was patterned on a glass substrate for FluidFM—as it relies on an inverted microscope—and on Si_3N_4-coated Si wafer for the samples printed by EHD-RP. An example of an AM line printed across one of 9 sets of electrodes—together with a schematic of the 4-terminal sensing configuration—is displayed in Fig. 1(d).

2.3 Printing on an insulating substrate—overcoming a paradox

Electrochemical techniques generally require a conductive path to supply the reduction current. A premature conclusion assumes that the two techniques are unable to print on the insulating areas of the substrate spanning between the contact electrodes. However, the electrons required for ions reduction are indirectly provided by a grounded electrode—where the first

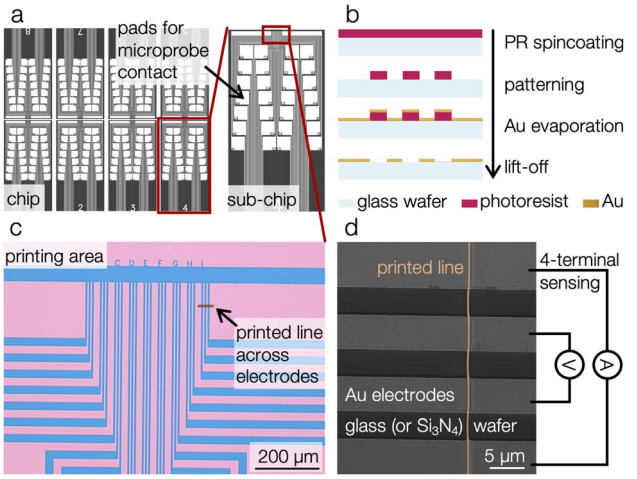

Fig. 1 Schematic of the electrode chip for electrical measurement and its fabrication process. (a) Mask design showing one electrode chip and a zoom-in of one of the 8 sub-chips. (b) Photolithography process. A spincoated glass or Si_3N_4 wafer is exposed and developed. A 3 nm titanium adhesion layer and a 25 nm gold layer are evaporated. The final lift-off reveals the 5 µm-spaced gold electrode tracks. (c) Optical microscope image of the patterned Si_3N_4 wafer in the sample testing areas (*i.e.* printing area). A printed line symbolically represented and spanning across a set of four electrodes illustrates the approach. (d) SEM micrograph showing a copper line printed across one set of measurement electrodes and schematic of the 4-terminal electrical characterization.

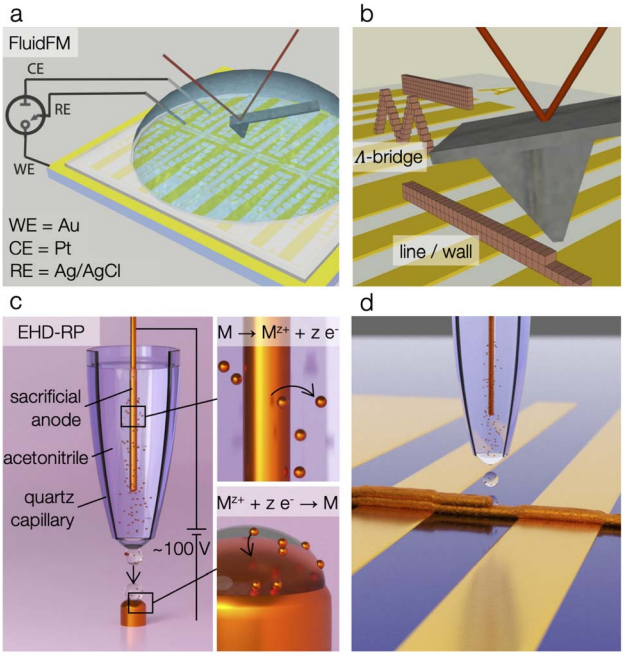

Fig. 2 Setup and working principles of (a) FluidFM and (c) EHD-RP and their respective printing strategies ((b) and (d)). (a) The chip substrate (yellow) is laminated with PDMS (white, transparent) to confine the supportive electrolyte droplet. The Pt and Ag/AgCl electrodes are inserted in the droplet cell and, together with the chip substrate (WE) connected to a potentiostat. The FluidFM probe is fully immersed inside the droplet cell. (b) Copper ions are extracted from the hollow AFM tip, reduced locally and, due to the integrated force-feedback (AFM laser path shown in red), the copper structures are printed in a voxel-by-voxel manner across the gold electrode tracks. During printing across the insulating regions, the previously printed voxel serves as local WE. (c) A metal sacrificial anode is immersed in an acetonitrile-filled capillary. A potential difference applied between the anode and the substrate triggers the anode corrosion and leads to the release of solvated metal ions M^{z+}. Ion-loaded droplets are ejected from the capillary nozzle. Upon landing on the grounded substrate, ions are reduced while the solvent evaporates, giving rise to the deposition of a metal voxel. (d) Double line printing strategy across the 4-terminal patterned substrate.

voxel is deposited—through the ongoing printed line, circumventing this issue.

Thus, conductive structures were successfully fabricated across the Si_3N_4 dielectric regions—spanning between the gold thin-film electrodes—both by FluidFM (Fig. 3) and EHD-RP (Fig. 4). The strategies employed by FluidFM for the structures visible in Fig. 3(b)–(e) consist in lateral print head movements in order to deposit voxels side by side (Fig. 2(b)). This strategy was employed to print either single or multiple layers, and the resulting structures will be referred to as line and wall, respectively. These results prove the potential of the two techniques to print micro- and submicrometer-sized interconnects across insulator gaps. Nevertheless, some of the results—in particular the line break seen in Fig. 3(d)–(e) and S1,† as well as the line constriction seen in Fig. 3(b) and (c)—illustrate important challenges arising from the topological and electrical inhomogeneity of the substrate. Namely, the presence of the electrode films influences the electric field in a way that the field lines bow towards the small radius of curvature at the film edges. Consequently, this phenomenon affects both the droplet trajectory in EHD-RP and the ion migration in FluidFM, and ultimately leads to the apparent line irregularity in the vicinity of the edges. This challenge is inherent to all microscale AM techniques that involve electric fields as a driving force for mass transport. Thus, we present various print strategies with both FluidFM and EHD-RP printing techniques to establish a baseline and fundamental insights for conductivity in electrically driven microscale AM.

2.4 Printing strategies

2.4.1 FluidFM. The strategy presented in Fig. 2(b) for FluidFM allows to circumvent the metal–insulator transition on the substrate by creating overhanging structures.[35] Each fabricated bridge consists in pairs of two out-of-plane 45° pillars leaning towards one another and meeting above the center of the dielectric gap between two electrodes. For this strategy—which will be referred to as "Λ-bridge"—the pillars are fabricated one after another and, subsequently, a final and unique link voxel is added. The success of this approach is visible in Fig. 3(f)–(h). Each voxel has a height of 200 nm, building up the bridges up to a final height of 6.3 µm, and a total lateral span of 33 µm. All structures were printed at −0.67 V (*vs.* Ag/AgCl) with a 500 Pa overpressure and the fabrication time was ≈10 min per structure. Despite using identical printing parameters, individual object dimensions vary slightly. Amongst five samples, printed with identical parameters, diameters ranged from 0.75 µm to

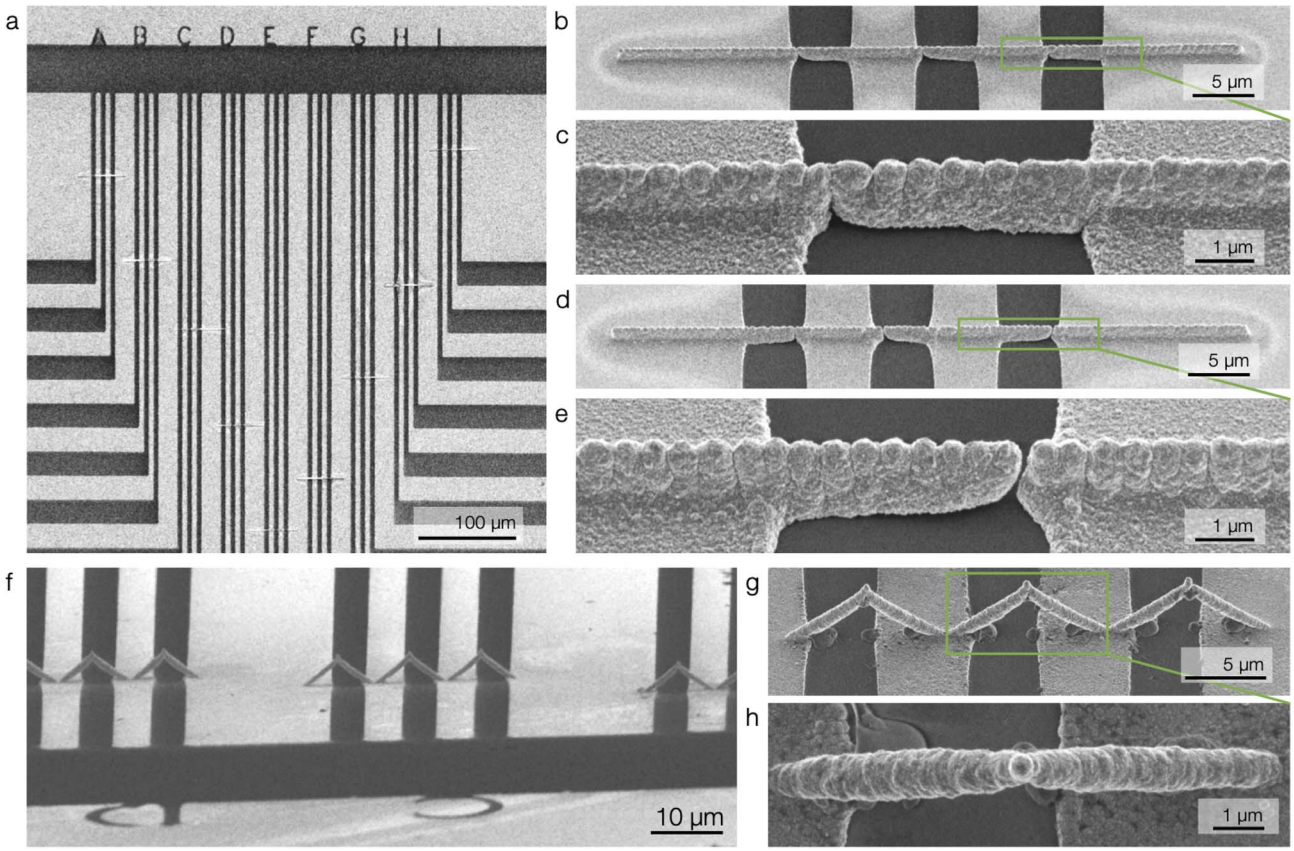

Fig. 3 SEM micrographs of 60 μm copper lines printed by FluidFM at −0.67 V (*vs.* Ag/AgCl). (a) Overview of 9 lines spanning across various sets of 4-terminal measurement electrodes. One of them is represented in (b) and shows a successful connection between the gold electrodes, as later confirmed by electrical characterization. (c) Enlarged view of a 5 μm long gap. The line in (d) and the zoom-in in (e) display a line printed with similar parameters but disconnected. (f) SEM images of a partial overview of 3D printed Λ-bridges spanning over glass tracks (dark grey). (g) Λ-bridge construction spanning over the 4 contact electrodes and (h) enlarged top-view of the central arc. Substrate tilts were respectively 45° for (b–e and g), 70° for (f), and 0° for the rest.

1.19 μm. Nevertheless, the printing process was significantly more stable compared to the in-plane line fabrication Fig. 3(h). We did not optimize the angle of the Λ-bridge, nonetheless we would like to emphasize that it can *a priori* span between 0° and 90° as previously shown.[35]

2.4.2 EHD-RP. The nozzle-to-substrate distance is the key processing parameter influencing the conformity of the deposited line at the gold electrode–Si_3N_4 transition. Lowering this parameter implies by definition a shorter droplet flight and, in consequence, reduced droplet deviation from a vertical path. Thus, while the previously reported distance was in the 7–10 μm range,[12,32] in this study the nozzle was kept as close as 3 μm from the substrate. Deposited line height is generally 300 nm or 1/10 of the substrate to nozzle height. At this constant distance and a 4 μm s^{-1} lateral speed, conductive copper lines composed of two layers (Fig. 2(d)) were printed across the sets of gold electrodes using different voltages. 9 of the 18 fabricated structures considered in the scope of this study are visible in Fig. 4(a) (printed at 95, 100 and 105 V), while the others (printed at 85, 90 and 95 V) were deposited on another equivalent printing area of the chip. Although the structure appears to span uninterruptedly over the 9 sets of measurement electrodes, it actually consists of 9 distinct lines (Fig. 4(b)) printed using 95, 100 and 105 V as a printing voltage (3 lines per voltage). The two layers composing each line are deposited within ≈15 s. While this strategy proves to be effective for the synthesis of lines with printing voltages of 90 V and above, the ones printed with lower voltage (85 V) still display a clear constriction at the gold electrode edge (Fig. 4(c) and (f)). Since this detrimental feature had been associated with interconnect failure during electrical characterization as a consequence of a local increase in current density, and in order to treat each line equally as a matter of consistency, all electrode transitions were covered with a conductive carbon pad deposited by FEBID, similar to the ones seen in Fig. 4(d). Arguably, this procedure does not invalidate the claim to successfully print conductive lines across insulator gaps since only the ones printed at 85 V strictly require it. Thus it was solely employed to enable the electrical characterization of all deposited structures.

2.5 Morphology, microstructure and resistivity

2.5.1 FluidFM. As presented in the introduction, surface morphology and microstructure are two important attributes influencing the electrical resistivity of micrometer-sized

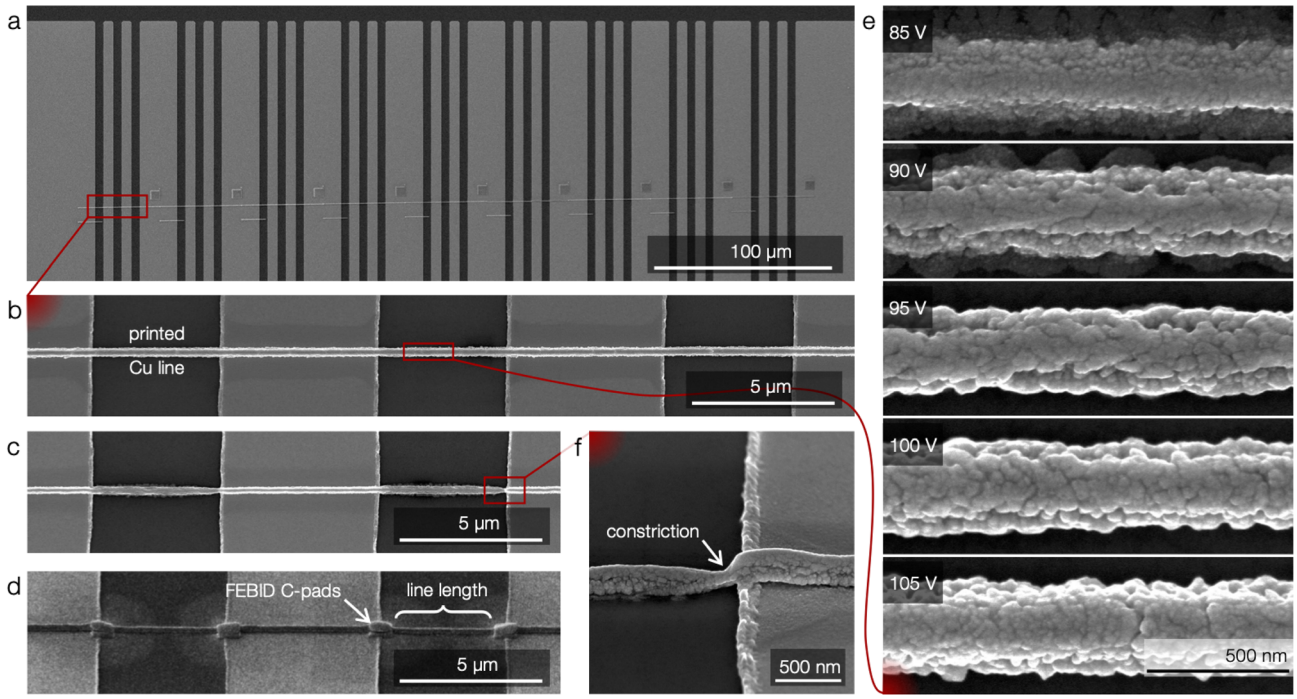

Fig. 4 SEM micrographs of sub-micrometer copper lines printed by EHD-RP across the substrate design for 4-terminal-measurement. (a) Overview of the lines across the 9 sets of measurement electrodes using different printing voltages. (b) Enlarged view on a line printed at 105 V and showing a homogeneous section along its length. (c) Line printed at 90 V showing variation in its width and, in particular, (f) a constriction at the transition between the dielectric and conductive substrate. (d) Same line as (c) on which carbon pads were deposited by ion beam-induced deposition to enhance electrical contact reliability. (e) Collection of SEM micrographs showing the direct influence of the printing voltage on the line morphology. Substrate tilts: (a–c and e) 0°, (d) 52°, (f) 55°.

conductors. In the structures deposited by FluidFM it appears that the printing strategy significantly influences the morphology: the in-plane lines and walls develop a bumpy top (Fig. 5(a) and (b)) but also overall a rough and inhomogeneous surface (Fig. 3(b)–(e)), whereas the Λ-bridges (Fig. 3(g) and (h) and Fig. 5(c)) appear more homogeneous. With regards to the inner structure, longitudinal focused ion beam (FIB) cross-sections reveal a polycrystalline microstructure in all FluidFM structures (Fig. 5(a)–(c)). For the in-plane structures, the grain size appears larger compared to the Λ-bridges (140 ± 30 nm (wall) and 130 ± 70 nm (line) *vs.* 70 ± 20 nm). Interestingly, the presence of pores is visible in the in-plane structures (Fig. 5(a) and (b)), while the Λ-bridge investigated appears fully dense (c). Such a difference concerning both the grain size and the presence of voids is possibly related to the different orientations of the Cu^{2+} cloud ejected from the probe aperture with respect to the surface of the previously electrodeposited voxel in the in-plane and bridge configurations. The detrimental effect of the pores on materials resistivity is further illustrated in the electrical measurement (Fig. 5(d)) which shows that the in-plane lines—despite their larger grain size—conduct around 2× less efficiently than the Λ-bridges: 62–84 μΩ cm *vs.* 13–51 μΩ cm (30 μΩ cm on average from 5 structures). For the Λ-bridges, the grain size (70 ± 20 nm) is on the order of the electron mean free path, thus grain boundaries are expected to be a significant source of electron scattering. The resistivity values measured for the 5 Λ-bridges (13.2 ± 1.9 μΩ cm to 51.3 ± 4.2 μΩ cm) correspond to 7.8× to 30× bulk copper. Compared to other copper structures printed with EC techniques, three out of five resistivity values are slightly lower than reported for MCED (31.5 μΩ cm),[27] including nt-copper (39.0 μΩ cm),[27,30] one is slightly above and our lowest reported value is somewhat lower than for EHD-RP (14.4 ± 2.1 μΩ cm).[32] The highest outlier can be explained by the shorter measured pillar's length, leading to a higher resistivity.

2.5.2 EHD-RP. For EHD-RP, copper lines were deposited using a unique strategy while varying the voltage applied to the sacrificial anode to assess the influence of this parameter. Surface details of the lines are visible in Fig. 4(e) and seem to consist of collated grains, the size of which is influenced by the voltage: larger ones (≈100 nm) for the intermediate voltage values (90–100 V) and smaller ones (≈50 nm and ≈20 nm) for the highest (105 V) resp. the lowest value (85 V) in the voltage space considered. This microstructure evolution with deposited voltage is in agreement with previous literature and is presumably linked to the continuous (*vs.* discontinuous) presence of solvent at the growth interface.[12] According to this reference, the reduced solvent ejection rate at low voltage (close to the limit of EHD ejection) leads to intermittent solvent drying which favors the renucleation of grains. At intermediate voltage, the deposition conditions would allow optimal grain growth, while further increase in voltage would again decrease the grain size—and increase the porosity—due to the increase in both the current density and the electric field at the growth surface.

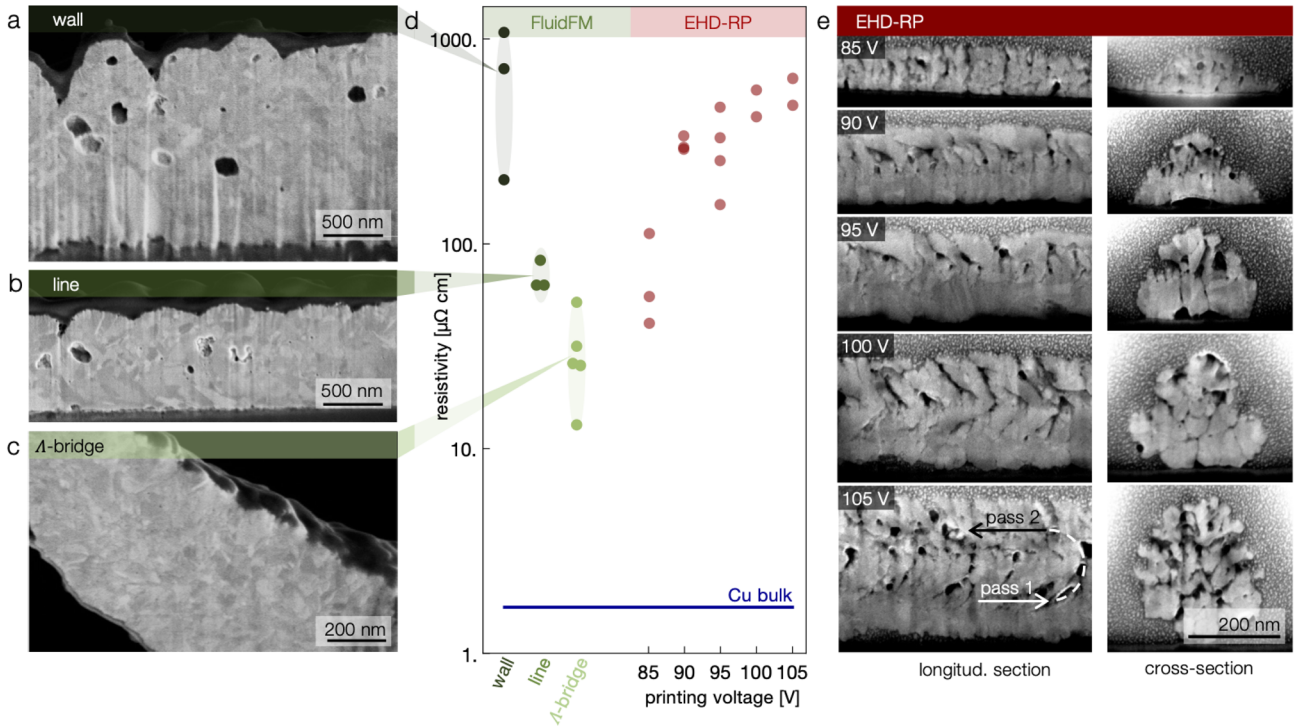

Fig. 5 Microstructure and electrical resistivity. (d) Measured electrical resistivity resulting from the different printing strategies of FluidFM (shades of green) and EHD-RP (wine-red) and comparison to bulk copper. Each datapoint represents the characterization of a different structure. (a–c and e) Associated representative microstructures unveiled by tilt-corrected micrographs of FIB-machined cross-sections. (a) Wall, (b) line and (c) Λ-bridge printed by FluidFM. (e) Compilation of longitudinal- and cross-section tilt-corrected images of double-pass lines fabricated by EHD-RP with increasing printing voltages.

Longitudinal and axial FIB cross-sections (Fig. 5(e)) unveil a non-trivial behavior of the microstructure evolution. At 95 V, the lines show two distinct parts: a dense polycrystalline microstructure at the bottom and a top part consisting of loosely-packed copper crystallites. Due to its low connectivity, the top part is not expected to allow significant electron mobility. With increasing printing voltage (100 and 105 V), the fraction of dense materials at the bottom decreases and thus a larger fraction of porous microstructure with disconnected grains is visible. Alternatively, compared to 95 V, the line printed using a 90 V anode potential has a similar microstructure, except for the grain size in the dense bottom part which appears smaller. Finally, the line printed with the lowest voltage (85 V) is composed of smaller grains (≈30 nm) with relatively poor intergranular connectivity.

The evolution in microstructure directly translates into changes in electrical properties. The decrease in resistivity observed when reducing the printing voltage from 105 V to 95 V correlates with the perceived decrease in porosity. On the other hand, a further reduction in voltage to 90 V does not significantly decrease resistivity compared to 95 V, which can be explained by the smaller grain size in the bottom part of the line. The lowest resistivity is obtained for the lowest printing voltage (85 V) despite the substantial porosity and small grain size (≈20 nm), and could be related to a more continuous percolation path in three dimensions compared to the other microstructures. Thus, further efforts—facilitated by the novel substrate design—are required to understand the relation between microstructure synthesized by EHD-RP and electrical resistivity.

The values presented here—24× to 400× larger than bulk copper—demonstrate how easily materials properties can be tuned by variation in the deposition parameters, for instance the voltage. On the one hand, it is of great importance because it offers an additional degree of freedom in materials design and unlocks the potential for the synthesis of micro-objects with optimized property distribution. On the other hand, those resistivity values are significantly higher than the one reported by Reiser *et al.* (8.6× larger than bulk).[32] This suggests there still exists room for microstructure improvement. Let us finally mention that bridge-like geometries have the potential for further improvement in the microstructure, but their fabrication remains challenging due to the autofocusing effect, which is exacerbated by the small feature size.

3 Conclusions

In this study, we have presented a lithography-based substrate design conceived for the direct electrical characterization of metal microstructures fabricated by two different electrochemical microscale AM techniques. The standardized design allows for comparable measurements between the various microstructures, whilst the lithography-based approach permits the characterization of a multitude of structures. In this

manner not only the materials' optimization procedure is enabled, but also a direct comparison between the micro AM techniques is facilitated. To illustrate this, we have reported on the direct fabrication of conductive metal structures spanning across the 4-terminal sensing setup both using FluidFM and EHD-RP techniques. For FluidFM, three different printing strategies (line, wall and Λ-bridge) were demonstrated and their influence on the connection reliability, microstructure and resistivity was discussed. In these regards, the Λ-bridge—a truly out-of-plane structure—leads to the lowest resistivity down to 13.2 ± 1.9 μΩ cm, comparable to values reported in literature for similar EC-based techniques. For EHD-RP the focus is set on the facile materials optimization process allowed by the substrate-based electrode approach. By varying the printing voltage from 85 to 105 V, the electrical resistivity can be tuned by an order of magnitude (41 to 640 μΩ cm) as a consequence of the microstructural changes. In general, synthesis techniques such as EHD-RP and FluidFM have the advantage to allow for more freedom in microstructure design: the materials being synthesized *in situ*, its characteristics are directly impacted by the processing parameters.

4 Experimental

4.1 Substrate fabrication

Electrode fabrication was achieved *via* a standard lithography process involving a lift-off step after the deposition of a titanium adhesion layer and a gold film *via* thermal evaporation. For this purpose, double side polished 3-inch borosilicate wafers (FluidFM) and 300 nm Si_3N_4-coated (111) Si wafers (EHD-RP) were used. Wafers, photoresists and resist remover were purchased from Microchemicals GmbH (Germany), other chemicals were obtained from Sigma Aldrich (USA). Details of the substrate fabrication process are shown in ESI Fig. S4.†

4.2 Chemicals used for printing

4.2.1 FluidFM. Printing ink consisted of a 0.5 M copper sulfate solution prepared by dissolution of copper sulfate ($CuSO_4$, Sigma Aldrich, USA) in 1 M H_2SO_4 (Sigma Aldrich, USA). The supportive electrolyte was obtained by mixing minute drops of H_2SO_4 (Sigma Aldrich, USA) with Milli-Q water until a pH of ≈3 was reached. All solutions were filtered through a 0.1 μm (ink) or 0.22 μm (supporting electrolyte) PVDF membrane (MilliporeSigma, USA) to minimize clogging and contamination.

4.2.2 EHD-RP. The sacrificial anode consisted of a high-purity copper wire (0.25 mm diameter, Puratronic® 99.9999%, AlfaAesar) that was etched for 10 s in concentrated nitric acid (35%, Sigma Aldrich) and subsequently rinsed with high-purity water (Optima™, Fisher Chemical). The sacrificial anode was inserted in a quartz capillary (QF100-70-15, Sutter Instrument) filled with high-purity acetonitrile (EMSURE® ACS, Sigma-Aldrich).

4.3 Print head fabrication

4.3.1 FluidFM. Standard FluidFM nanopipette probes (Cytosurge AG, Switzerland) with a nominal spring constant of 2 N m^{-1} and a pyramidal tip with a 300 nm aperture at the apex, were used as printing nozzles. Prior to use, the probe was plasma treated for 2 min at 180 W (PDC-002, Harrick Plasma, USA) to enhance the filling of the integrated microfluidic channel. After plasma treatment, 10 μL of the filtered $CuSO_4$ ink was pipetted into the probe's reservoir, which was sealed off with a FluidFM Pneumatic Connector (Cytosurge, Switzerland). Next, positive pressure was applied to the reservoir to load the cantilevers' inner microfluidic channel with the printing ink. After deposition, functioning probes were immersed in a well (24-well plate, TPP, Switzerland) and stored in a fridge for further use.

4.3.2 EHD-RP. Micropipettes used in the EHD-RP setup were fabricated from quartz capillaries (QF100-70-15, Sutter Instrument) using a micropipette puller (P-2000, Sutter Instrument). Typical pulling parameters were: line 1, heat = 810, fil = 5, vel = 30, del = 128, pull = 50; line 2, heat = 700, fil = 4, vel = 50, del = 130, pull = 75 and lead to opening diameters ≈180 nm. The nozzle used in this study had an inner diameter of 185 nm, as measured by scanning electron microscopy.

4.4 Printing procedure

In preparation for printing, electrode chips were cleaned in an ultrasonic bath for 10 min in acetone, 10 min in IPA, and blow-dried with the nitrogen gun. Post-printing, all samples were stored in Gel-Box™ (Gel-Pak, USA) under vacuum conditions.

4.4.1 FluidFM. Printing was performed inside a droplet-based electrochemical cell which consisted of the electrode chip as working electrode, a Pt wire as counter electrode and an Ag/AgCl coated wire as quasi-reference electrode. A thin PDMS ring was ultrasonicated in IPA for 5 min, flushed with Milli-Q water, blow-dried under a nitrogen stream, and carefully placed on top of the electrode surface. Approximately 250 μL droplet of supportive electrolyte was then pipetted inside the PDMS ring. The Pt and Ag/AgCl wires were rinsed with IPA and water prior to use and were glued with UV glue (Loctite AA 3301, Henkel Adhesives, Germany) to the FluidFM pneumatic connector. After printing, the droplet of supportive electrolyte was removed and the electrode substrate was flushed with Milli-Q water and blow-dried under a nitrogen stream.

4.4.2 EHD-RP. The prepared sacrificial anode was inserted in a quartz micropipette filled with high-purity acetonitrile (EMSURE® ACS, Sigma-Aldrich) and was subsequently introduced in the micro-printing setup above the printing substrate. The printing chamber was flushed with argon to decrease the oxygen partial pressure below 50 ppm. The copper lines consisted of two layers, each of which printed with a 4 μm s^{-1} substrate movement and a constant printing voltage between 85 and 105 V. The distance between the nozzle and the substrate was maintained at 3 μm. Due to the imperfect coplanarity between the substrate plane and the in-plane piezo movement, this distance was continuously corrected by the vertical piezo stage. The structures were printed without interruption, while

a 6 × 6 μm^2 pad (visible in Fig. 4(a)) was printed for 60 s between two lines in order to reach the new equilibrium in case of a voltage change.

4.5 Microprinting set-up

4.5.1 FluidFM. The microprinting setup is a FluidFM system consisting of a FluidFM probe mounted onto an AFM scanning head (Nanowizard 1, JPK Bruker, Germany). The system is placed on top of an inverted microscope (Axiovert MAT 40, Zeiss, Germany) operated in darkfield mode, which enables live monitoring of the EC printing. Soft Tygon tubing (0.76 mm ID, Ercatech, Switzerland) connects the FluidFM probe to an MCFS 4C pressure controller (Fluigent, France). All aforementioned hardware components are controlled by an in-house built LabVIEW program using two data acquisition cards (NI USB 6343, National Instruments, USA). The potential inside the electrochemical cell is controlled manually (PGU10V-1A, IPS Jaissle, Germany). The LabVIEW program interprets the variation in the AFM photodiode signal as the completion of a voxel, and uses it as a growth feedback to trigger the probe movement to the next voxel position. Printing instructions containing the spatial coordinates, as well as desired pressure for each voxel, are either generated by a LabVIEW program or created in .csv format with a custom Python code.

4.5.2 EHD-RP. The EHD-RP microprinting setup consists of a 3-axis nanopositioning stage (QNP60XY-500-C-MP-TAS, QNP60Z-250-C-TAS, Aerotech), a solvent-filled quartz nanopipette containing a copper sacrificial anode connected to a power source (B2962A, Keysight), a grounded substrate and a light microscope system. The setup lies in a closed chamber which is flushed with argon before printing. The stage movement and the anode potential were controlled and monitored using a MATLAB script developed in-house and running on a desktop computer.

4.6 IV measurements

Electrical resistance of the printed structures was assessed using a microprobe station equipped with four microprobe positioners (Karl Suess (Now: SUSS MicroTec), Germany) and a device parameter analyzer (Agilent (now: Keysight) B1500A Semiconductor Device Parameter Analyze, Keysight, USA) controlled with EasyEXPERT software. The measurement setup is installed inside a Faraday cage for shielding and noise reduction. Prior to measurement, the printed structures were electrically disconnected from the rest of the gold substrate by scratching the connecting electrode tracks with a diamond pen. IV curves of the samples were obtained in a 4-terminal configuration by performing a sweep between positive and negative voltage values. Starting at 5 mV, the amplitude of the sweep (performed 3 times for each step) was increased in steps of 5 mV until the non-linear regime was reached. The line resistance was derived as the slope of a linear function fitted to the IV data in the linear regime (ESI Fig. S2 and S3†). Resistivity was then derived as $\rho = RA/l$, with R the resistance, A and l respectively the cross-sectional area and the length of the line as defined in the experimental section on geometrical characterization.

4.7 Electron microscopy analysis and characterization

4.7.1 FluidFM. SEM images of the printed structures were obtained with a JSM-7100F SEM (JEOL, Japan) microscope, using an acceleration voltage of 2 kV and a stage tilt of 0°, 45° or 75°. Post-IV analysis, the samples were coated with a 5 nm carbon layer (CCU-010 HV, Safematic, Switzerland) to prevent sample charging. Cross-sections of the printed structures were achieved by FIB milling (Helios 5UX DualBeam, Thermofisher Scientific, USA), with currents between 7 pA (polishing) and 0.26 nA (coarse milling). The cross-sections were imaged at 2 kV in SEM immersion mode using an in-lens detector. Obtained images were not tilt-corrected unless stated otherwise.

4.7.2 EHD-RP. SEM images were acquired with a FEI Magellan 400 microscope (Thermofisher Scientific, USA) in immersion mode with an acceleration voltage of 5 kV and a stage tilt of 0° or 55°. Cross-sections were achieved by FIB milling (Helios 600 i FIBSEM, Thermofisher Scientific, USA) using a 7 pA current. The cross-sections were imaged at 5 kV in immersion mode using in-lens detector. Obtained images were not tilt-corrected unless stated otherwise.

4.8 Geometrical and microstructural characterization

4.8.1 FluidFM. The dimensions of the printed structures were retrieved as follows. For the printed lines and walls, the both length and width were determined from SEM topview (0° tilt) images. The length was taken as the electrode track separation and remained consistent throughout the measurements (5 μm). The height was measured from images taken at 45° stage tilt, and the value was corrected for the tilt. The cross-sectional area of the lines was approximated as a semi-ellipse, whereas the walls were assumed to have a rectangular shape. The average width of the leaning pillars was approximated from SEM top-view images by measuring at 10 different sections along the structure. Additionally, the width of the constriction was obtained from the same SEM image. The total length was determined from tilt-corrected FIB SEM (operated in SEM mode) images. The length and height of the constriction were retrieved from tilt-corrected (FIB) SEM images of the pillar's longitudinal cross-section. For the cross-sectional area calculations, an elliptical profile of the constriction was assumed, whilst the leaning pillars were approximated by cylinders. All measurement errors were propagated during the resistivity calculations. The grain size distribution was derived using Lince Linear Intercept 2.4.2β by manually identifying the interception of grain boundaries with multiple lines of random orientation.

4.8.2 EHD-RP. The line length was taken as the distance between two deposited FEBID pad, while the cross-sectional areas were obtained from tilt-corrected FIB-machined cross-section SEM images (Fig. 5(e)) using the color threshold feature of imageJ. The porosity was not included in the area, thus an effective cross-section was considered. One cross-sectional area measurement was performed for each line. All images were analyzed using ImageJ (ImageJ, National Institutes of Health, USA).

Author contributions

Maxence Menétrey: investigation, methodology, software, formal analysis, visualization, writing – original draft, Cathelijn van Nisselroy: investigation, methodology, software, formal analysis, visualization, writing – original draft, Mengjia Xu: investigation, methodology, software, Julian Hengsteler: investigation, Ralph Spolenak: supervision, writing – review & editing, funding acquisition, Tomaso Zambelli: supervision, writing – review & editing, funding acquisition.

Conflicts of interest

There are no conflicts to declare.

Acknowledgements

Processing of the lithography masks was performed by Dirk van Swaay (Wunderlichips GmbH). Both scanning electron microscopy and focus ion beam milling was conducted at ScopeM, the microscopy platform of ETH Zürich. The authors would like to thank Joakim Reuteler from ScopeM for his assistance. Aldo Rossi (ETH Zürich, D-ITET) is acknowledged for his technical support in the cleanroom and for thermal evaporation of gold layers onto the sample substrates. Furthermore, the authors gratefully thank Christian Vogt (ETH Zürich, D-ITET) for his support regarding the IV measurements. The authors also thank Souzan Hammadi for her insightful preliminary work on the printing optimization of conductive lines by EHD-RP. The authors gratefully acknowledge Rebecca Gallivan for her valuable feedback on the manuscript. The work by M. M. and R. S. was funded by the SNF Grant 200021_188491. The contribution of C. v. N. and T. Z. was financially supported by the Swiss Agency for Technology and Innovation Innosuisse, Project No.: PNFM-NM 18511.1.

Notes and references

1 L. Hirt, A. Reiser, R. Spolenak and T. Zambelli, *Adv. Mater.*, 2017, **29**, 1604211.
2 M. Carlotti and V. Mattoli, *Small*, 2019, **15**, 1902687.
3 N. Zhou, C. Liu, J. A. Lewis and D. Ham, *Adv. Mater.*, 2017, **29**, 1605198.
4 J. Schneider, P. Rohner, D. Thureja, M. Schmid, P. Galliker and D. Poulikakos, *Adv. Funct. Mater.*, 2016, **26**, 833–840.
5 G. Arnold, R. Winkler, M. Stermitz, A. Orthacker, J.-H. Noh, J. D. Fowlkes, G. Kothleitner, M. Huth, P. D. Rack and H. Plank, *Adv. Funct. Mater.*, 2018, **28**, 1707387.
6 J. Sattelkow, J. E. Fröch, R. Winkler, S. Hummel, C. Schwalb and H. Plank, *ACS Appl. Mater. Interfaces*, 2019, **11**, 22655–22667.
7 D. Gall, *J. Appl. Phys.*, 2016, **119**, 085101.
8 D. Josell, S. H. Brongersma and Z. Tőkei, *Annu. Rev. Mater. Res.*, 2009, **39**, 231–254.
9 A. F. Mayadas and M. Shatzkes, *Phys. Rev. B: Solid State*, 1970, **1**, 1382–1389.
10 R. S. Smith, E. T. Ryan, C.-K. Hu, K. Motoyama, N. Lanzillo, D. Metzler, L. Jiang, J. Demarest, R. Quon, L. Gignac, C. Breslin, A. Giannetta and S. Wright, *AIP Adv.*, 2019, **9**, 025015.
11 A. Reiser, L. Koch, K. A. Dunn, T. Matsuura, F. Iwata, O. Fogel, Z. Kotler, N. Zhou, K. Charipar, A. Piqué, P. Rohner, D. Poulikakos, S. Lee, S. K. Seol, I. Utke, C. van Nisselroy, T. Zambelli, J. M. Wheeler and R. Spolenak, *Adv. Funct. Mater.*, 2020, **30**, 1910491.
12 M. Menétrey, L. Koch, A. Sologubenko, S. Gerstl, R. Spolenak and A. Reiser, *Small*, 2022, **18**, 2205302.
13 M. A. Skylar-Scott, S. Gunasekaran and J. A. Lewis, *Proc. Natl. Acad. Sci. U. S. A.*, 2016, **113**, 6137–6142.
14 P. Galliker, J. Schneider, H. Eghlidi, S. Kress, V. Sandoghdar and D. Poulikakos, *Nat. Commun.*, 2012, **3**, 890.
15 K. Rahman, A. Khan, N. M. Muhammad, J. Jo and K.-H. Choi, *J. Micromech. Microeng.*, 2012, **22**, 065012.
16 B. W. An, K. Kim, H. Lee, S.-Y. Kim, Y. Shim, D.-Y. Lee, J. Y. Song and J.-U. Park, *Adv. Mater.*, 2015, **27**, 4322–4328.
17 N. C. Schirmer, T. Schwamb, B. R. Burg, N. Hotz and D. Poulikakos, *Appl. Phys. Lett.*, 2009, **95**, 033111.
18 P. Rohner, A. Reiser, F. T. Rabouw, A. S. Sologubenko, D. J. Norris, R. Spolenak and D. Poulikakos, *Nanoscale*, 2020, **12**, 20158–20164.
19 N. Zhou, C. Liu, J. A. Lewis and D. Ham, *Adv. Mater.*, 2017, **29**, 1605198.
20 J. J. Adams, E. B. Duoss, T. F. Malkowski, M. J. Motala, B. Y. Ahn, R. G. Nuzzo, J. T. Bernhard and J. A. Lewis, *Adv. Mater.*, 2011, **23**, 1335–1340.
21 B. Y. Ahn, E. B. Duoss, M. J. Motala, X. Guo, S.-I. Park, Y. Xiong, J. Yoon, R. G. Nuzzo, J. A. Rogers and J. A. Lewis, *Science*, 2009, **323**, 1590–1593.
22 S. Lee, M. Wajahat, J. H. Kim, J. Pyo, W. S. Chang, S. H. Cho, J. T. Kim and S. K. Seol, *ACS Appl. Mater. Interfaces*, 2019, **11**, 7123–7130.
23 J. Wang, R. C. Y. Auyeung, H. Kim, N. A. Charipar and A. Pique, *Adv. Mater.*, 2010, **22**, 4462–4466.
24 C. W. Visser, R. Pohl, C. Sun, G.-W. Römer, B. Huis in 't Veld and D. Lohse, *Adv. Mater.*, 2015, **27**, 4103.
25 A. P. Suryavanshi and M.-F. Yu, *Appl. Phys. Lett.*, 2006, **88**, 083103.
26 S. K. Seol, D. Kim, S. Lee, J. H. Kim, W. S. Chang and J. T. Kim, *Small*, 2015, **11**, 3896–3902.
27 D. Eliyahu, E. Gileadi, E. Galun and N. Eliaz, *Adv. Mater. Technol.*, 2020, 1900827.
28 Y. Lei, X. Zhang, D. Xu, M. Yu, Z. Yi, Z. Li, A. Sun, G. Xu, P. Cui and J. Guo, *J. Phys. Chem. Lett.*, 2018, **9**, 2380–2387.
29 J. Hu and M.-F. Yu, *Science*, 2010, **329**, 313–316.
30 A. Behroozfar, S. Daryadel, S. R. Morsali, S. Moreno, M. Baniasadi, R. A. Bernal and M. Minary-Jolandan, *Adv. Mater.*, 2018, **30**, 1705107.
31 L. Lu, Y. Shen, X. Chen, L. Qian and K. Lu, *Science*, 2004, **304**, 422–426.
32 A. Reiser, M. Lindén, P. Rohner, A. Marchand, H. Galinski, A. S. Sologubenko, J. M. Wheeler, R. Zenobi, D. Poulikakos and R. Spolenak, *Nat. Commun.*, 2019, **10**, 1853.

33 R. Garcia, A. W. Knoll and E. Riedo, *Nat. Nanotechnol.*, 2014, **9**, 577–587.
34 A. Meister, M. Gabi, P. Behr, P. Studer, J. Vörös, P. Niedermann, J. Bitterli, J. Polesel-Maris, M. Liley, H. Heinzelmann and T. Zambelli, *Nano Lett.*, 2009, **9**, 2501–2507.
35 L. Hirt, S. Ihle, Z. Pan, L. Dorwling-Carter, A. Reiser, J. M. Wheeler, R. Spolenak, J. Vörös and T. Zambelli, *Adv. Mater.*, 2016, **28**, 2311–2315.
36 G. Ercolano, C. van Nisselroy, T. Merle, J. Vörös, D. Momotenko, W. W. Koelmans and T. Zambelli, *Micromachines*, 2020, **11**, 6.